Three-dimensional refractive index distributions of individual angiosperm pollen grains

Chansuk Park[1,2], SangYun Lee[1,2], Geon Kim[1,2], SeungJun Lee[3], Jaehoon Lee[3], Taehyun Heo[3], Yoonjeong Park[3], and YongKeun Park[1,2,4*]

[1]*Department of Physics, Korea Advanced Institutes of Science and Technology (KAIST), Daejeon 34141, Republic of Korea*
[2]*KAIST Institute for Health Science and Technology, KAIST, Daejeon 34141, Republic of Korea*
[3]*Daedeok High School, Daejeon 34121, South Korea*
[4]*Tomocube, Inc., 48, Yuseong-daero 1184 beon-gil, Yuseong-Gu, Daejeon 34051, Republic of Korea*
Corresponding Author: yk.park@kaist.ac.kr

Three-dimensional (3D) refractive index (RI) imaging and quantitative analyses of angiosperm pollen grains are presented. Using optical diffraction tomography, the 3D RI structures of individual angiosperm pollen grains were measured without using labeling or other preparation techniques. Various physical quantities, including volume, surface area, exine volume, and sphericity, were determined from the measured RI tomograms of pollen grains. Exine skeletons, the distinct internal structures of angiosperm pollen grains, were identified and systematically analyzed.

Keywords: Optical diffraction tomography, Quantitative phase imaging, Label-free, Pollen grain, Angiosperm.

1. Introduction

Pollen grains are the male gametophytes of spermatophytes (seed plants), and they play a major role in the reproduction of various plants [1]. A pollen grain fertilizes a female gametophyte through cell-to-cell recognition and by sprouting its tube towards it. Studying various biological aspects of pollen grains has contributed to the development of multiple scientific fields. The evolution of seed plants is studied in paleontology [2], in plant ecology and reproduction [3], and in agricultural science, which focuses on plant breeding techniques [4].

Among various spermatophytes, angiosperm (flowering plant) pollen grains provide the most fruitful information regarding ecology. Angiosperms have the widest ecological niche on Earth through their active interaction with the surrounding environment during pollination. Through pollination, angiosperms influence their pollinators, including animals and insects, and even the entire ecosystem [5-7]. Therefore, the study of angiosperm pollen grains provides important clues for understanding the evolution of various species and the ecosystem.

One of the most intriguing features of angiosperm pollen grains is their morphology. The unique morphology of an angiosperm pollen grain is deeply related to its early development and survival in various environments [8-10]. There have been many attempts to study the morphology of angiosperm pollen grains. Previously, various imaging techniques were employed, including bright-field optical microscopy, scanning electron microscopy (SEM), transmission electron microscopy (TEM), fluorescence microscopy, and X-ray imaging [11-15]. However, conventional imaging techniques cannot facilitate quantitative analysis or maintaining the cell viability of a pollen grain.

Unfortunately, the abovementioned imaging techniques do not fully address three-dimensional (3D) information of pollen grains in their intact conditions. Bright-field microscopy restrictively provides low-contrast and qualitative two-dimensional (2D) imaging. TEM only provides a 2D image of a sliced sample. SEM yields 3D high resolution images of a sample, but it can only provide the surface information. Moreover, conventional techniques require either time-consuming preparation steps or complicated setups. Fixation and staining of a sample is often required for bright-field microscopy [16, 17]. Either metallic coating [11, 12] or nanometer-scale slicing [13] is required in SEM and TEM, respectively, which fundamentally limits live cell imaging using electron microscopy. Although fluorescence microscopy enables molecular-specific imaging [15, 18], the use of exogenous labeling agents compromises cell viability, resulting from phototoxicity and photodamaging [19]. Photobleaching of fluorescence proteins or dyes also prevents long-term measurements [20].

Recently, quantitative phase imaging (QPI) techniques have emerged as useful tools for label-free live cell imaging of biological samples [21, 22]. QPI exploits the refractive index (RI) of a sample as an intrinsic imaging contrast and provides unique advantages in imaging, facilitating label-free quantitative imaging of live samples [23]. Among them, optical diffraction tomography (ODT) reconstructs the 3D RI tomogram of a sample. ODT is an optical analog of X-ray computed tomography [24, 25]. In ODT, multiple 2D optical fields from a sample are measured at various illumination angles. This data is used to construct a 3D RI tomogram based on the theory of optical diffraction. 3D RI tomograms provide various quantitative information about biological samples, including cellular volume, dry mass, and protein concentration [13, 14]. ODT has been widely utilized for studying 3D structures of biological organisms, including neurons [26, 27], mammalian cells [25, 28, 29], red blood cells [30-33], eukaryotic cells [26, 34-36], immune cells [34, 37], bacteria [38-40], yeasts [41], and microalgae [42]. Recently, ODT was used to study the 3D structures of Pinus pollen grains and addressed air bag structures in grains [43]. However, label-free imaging of angiosperm has not been performed in the past.

Here we present 3D RI imaging and quantitative analyses of angiosperm pollen grains using ODT. Angiosperm pollen grains of *Lilium candidum* (lily), *Iris domestica* (leopard lily), and *Hemerocallis dumortieri* (daylily) were imaged, and their distinctive structures were analyzed systematically. Furthermore, physical quantities of the pollen grains, including volume, exine volume, surface area, and sphericity, were retrieved from the measured 3D RI distribution of the samples. This approach is label-free, requires no sample preparation, and demonstrates the potential of ODT as a tool for 3D imaging and quantitative analysis in plant biology.

2. Methods

A commercial ODT setup based on off-axis Mach-Zehnder interferometry (HT-1S, Tomocube Inc., Republic of Korea) was used in this study (see Figs. 1(a) and 1(b)). A diode-pumped solid-state laser ($\lambda = 532$ nm) was used as an illumination source.
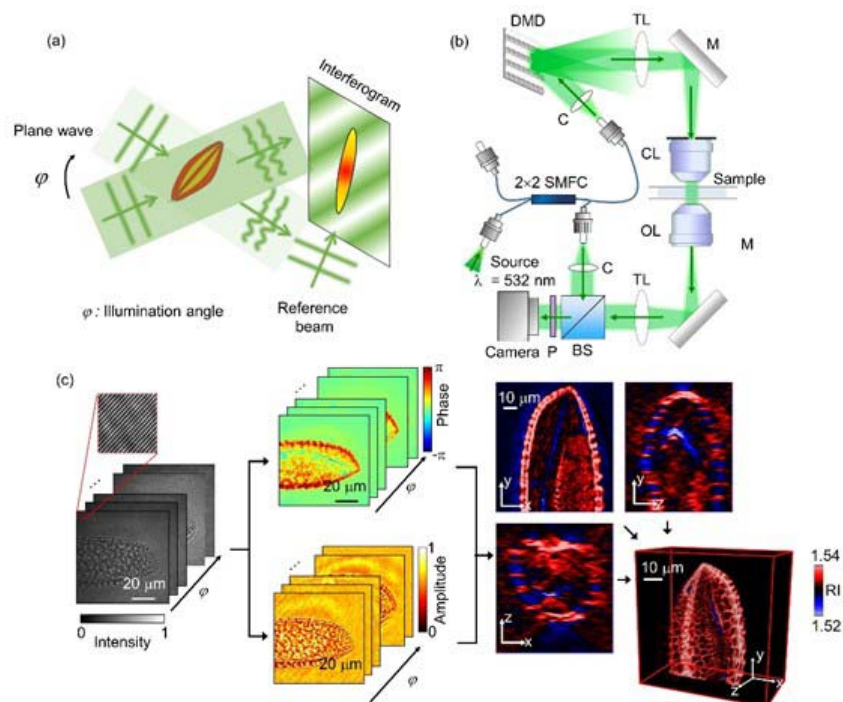

Figure 1: (a) Schematic diagram of the optical diffraction tomography (ODT) setup. The angle of illumination is rotated while the interferogram is recorded with the detector. (b) Optical setup for hologram measurement. 2×2 SMFC: single-mode fiber optic coupler, C: collimator, TL: tube lens, M: mirror, CL: condenser lens, OL: objective lens, BS: beam splitter, and P: polarizer. (c) Reconstruction procedure of the 3D RI distribution.

The beam from the illumination source was split into two arms. In a sample arm, a sample was illuminated with a plane wave, and the illumination angle was rapidly controlled using a digital micromirror device [44]. A beam scattered from a sample was projected to a camera plane with a 4-f telescopic imaging system consisting of an

objective lens (60× magnification, numerical aperture = 0.8) and a tube lens (f = 175 mm). A reference arm is also projected onto a sample plane at a prescribed tilt angle. Both the sample and reference arm interfere at the image plane, and the interferogram was recorded using a CMOS camera with 150 fps frame rate (FL3-U3-13Y3M-C, FLIR Systems Inc., USA) (see Figs. 1(a) and 1(b)). In total, 49 interferograms were recorded at various illumination angles requiring 0.4 s.

From a measured hologram, the 2D optical field image, consisting of both the phase and amplitude, was retrieved by applying a field retrieval algorithm based on Fourier transform (see Fig. 1(c)) [45]. According to the Fourier diffraction theorem [24], each 2D optical field corresponding to a specific illumination angle was mapped onto a corresponding Ewald surface in 3D Fourier space [24]. Then, the 3D RI distribution of a sample was finally obtained by applying inverse Fourier transform to the filled Fourier domain. The spatial resolution of the ODT system, as calculated from the achievable spatial bandwidth, is 166 nm and 1 μm for the lateral and axial directions, respectively [46, 47]. Due to the limited numerical apertures of both the condenser and objective lens, there exists scattering signals that cannot be collected, known as missing cone information. This missing cone information was filled using an iterative regularization algorithm based on non-negativity [48]. Detailed information on ODT can be found elsewhere [25, 49].

Pollen grains from *Lilium candidum* (lily), *Iris domestica* (leopard lily), and *Hemerocallis dumortieri* (daylily) were collected from a local botanical garden (Hanbat Arboretum, Daejeon, Republic of Korea) by rubbing stamens with a cotton swab. Before imaging, pollen grains were immersed into an RI-matching oil (Series A, Cargille Labs, United States) with n = 1.53 (for *L. candidum and I. domestica*) and n = 1.54 (for *H. dumortieri*) to prevent multiple light scattering within a sample. This ensures the reconstruction of 3D RI tomography in ODT, otherwise strongly scattering samples cannot be reconstructed [50]. Since the size of a sample exceeded the field of view of the imaging system (80.4 μm × 80.4 μm), each sample was imaged twice within adjacent fields of view. Then, the 3D RI distributions obtained from different parts of a sample were manually stitched after the reconstruction procedure.

Various physical quantities of individual pollen gains can be retrieved from the reconstructed 3D RI tomogram of samples, including volume, surface area, sphericity, and exine (pollen wall) volume. The exine skeletons were distinguished from the surrounding medium by applying RI thresholds of 1.533, 1.533, and 1.527 for pollen grains from *L. candidum*, *I. domestica*, and *H. dumortieri*, respectively. The RI threshold for the exine was manually chosen such that the exine substructures were the most visible. The total region occupied by pollen grains was calculated by filling the obtained exine skeletons using a custom script using MatLab^{TM}. The exine volume *E* and the total pollen grain volume *V* were quantified by multiplying the volume of a unit voxel (4.6×10^{-15} L) and the total number of voxels occupied by the according region. The surface area of a pollen grain *SA* was calculated using a similar method. Sphericity *S* was calculated using the equation

$$S = \left(36\pi V^2\right)^{1/3} / SA \,.$$

3. Results

The 3D RI distributions of pollen grains from three species of angiosperm plants were reconstructed using ODT. The 3D RI maps of the representative pollen grains for each species are shown in Fig. 2. The *x-y* cross-sectional images of the reconstructed RI tomograms are shown at various axial positions (z = -5, -2.5, 0, and 5 μm).

The measured RI tomograms of a pollen grain present characteristic morphological features, including exine and its substructures (tectum, columellae, and foot layer). Exine is the tough outer wall of a pollen grain and was identified as a web-like structure covering the cytoplasmic core ((i) in Fig. 2). The overall shape and size of the exine structure observed in the 3D RI tomograms are comparable to previous reports where SEM was used [9, 51-53]. Exine exhibits high RI values ranging from 1.53 to 1.54 compared to other structures. This can be explained by the fact that exine consists of sporopollenin [54], one of the most chemically stable biological polymers and a major component in the exine of plant spores and pollen grains.
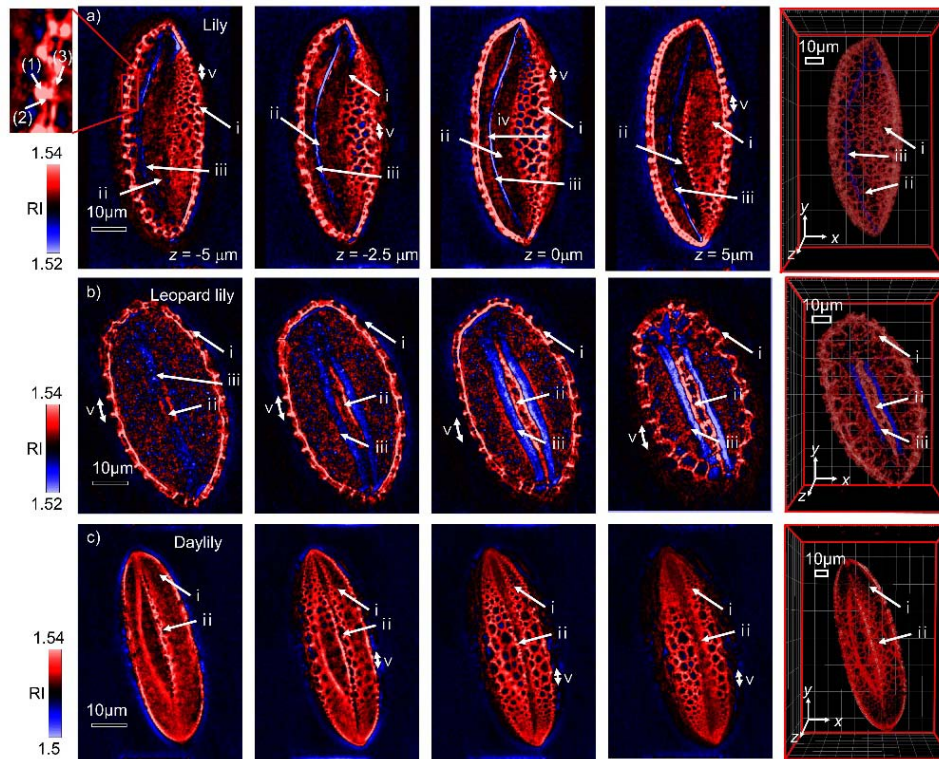
Figure 2: 3D Volume rendering of the sample RI distribution/cross-sectional images of pollen grains from (a) *L. candidum,* (b) *I. domestica,* and (c) *H. dumortieri.* Each column includes cross-sectional images from different axial depths. The rightmost column shows a 3D volume rendering of the RI distributions. Distinctive structures of the angiosperm pollen grain are shown, including (i) exine, (ii) pollen aperture, and (iii) the lower RI region, which are assumed to be endexine and intine. Substructures of the exine were recognizable, including (1) tectum, (2) columellae, and (3) foot layer. Physical quantities of the pollen grain were measured from the cross-sectional images, including (iv) depth of the fold and (v) tectum period.

The exine substructures, including tectum, columellae, and foot layer, were also visible, as highlighted in the red box in Fig. 2(a). Tectum, the outmost layer of the exine was observed as a roof of the exine wall. The tectum was periodically distributed along the tangential direction of the pollen surface, making the surface of the pollen grain rugged. Columellae is an intermediate layer between the tectum and the foot layer and was visualized as a column connecting the tectum to the foot layer. These exine substructures are consistent with results found with SEM [55].

The pollen aperture was identified, which is the site where a pollen tube reaches out during germination ((ii) in Fig. 2) [56]. Exine wall was observed to be folded inward along the aperture. The fold is created by a process known as harmomegathy [8], which prevents dehydration of pollen grains in an arid environment. A layer with an RI of 1.517, which is lower than a surrounding medium, was visible right next to the pollen aperture ((iii) in Fig.2). These layers are assumed to be endexine and intine structures, according to the anatomical information regarding the angiosperm pollen grains from previous studies [57]. The endexine is another exine substructure located beneath the foot layer, and the intine is the inner wall of the pollen grain.

Morphological features of the pollen grains were quantified from the measured 3D RI distributions. The pollen grains from three species of angiosperms were found to be ellipsoidal. The principal axis lengths of the lily pollen grain were measured to be 66.3 µm, 46.4 µm, and 33.2 µm in descending order. The thickness of the exine wall of a lily pollen grain was 3.9 µm and was manually measured from the cross-sectional image at $z = 0$. The depth of the exine fold (35 µm) of the lily pollen grain ((iv) in Fig. 2) was directly measurable from the cross-sectional image. The *L. candidum* pollen grain had principle axes with lengths of 82.6 µm, 49.3 µm, and 41.6 µm. The exine thickness was 3.7 µm. A pollen grain from *I. domestica* showed the most distinct view of the two exine walls in contact at the pollen aperture. Moreover, a distance between the two neighboring tecta ((v) in Fig.2) of the lily pollen grain was largest (13.6 µm) among the investigated pollen grains. *H. dumortieri*

pollen grain had the largest size among the three species, with principle axis lengths of 139.5 µm, 40.4 µm, and 29.9 µm. The exine thickness of the *H. dumortieri* pollen grain was 3.0 µm, which was the smallest value among the pollen grains from three species.
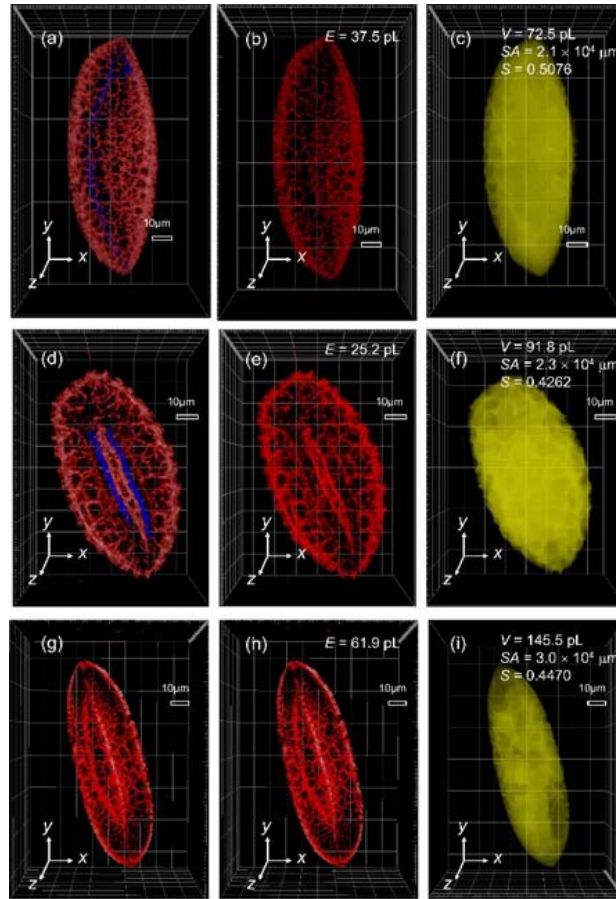

Figure 3: (a–c) 3D RI distribution of the pollen grains from three angiosperm species. (d–f) Exine skeletons separated by applying an appropriate RI threshold. The exine volumes E were obtained by multiplying the number of voxels occupied by the exine skeletons with the volume of a unit voxel. (g–i) Total space occupied by the pollen grains. The volumes (V) surface areas (SA) were obtained analogous to (b). Sphericity (S) of each pollen grain was calculated from V and SA.

Physical quantities including pollen grain volume *V*, surface area *SA*, sphericity *S*, and exine volume *E* were retrieved from the 3D volumetric information. Five pollens from *I. domestica*, two pollens from *L. candidum*, and one pollen from *H. dumortieri* were measured and analyzed. The representative tomograms are shown in Fig. 3. The space occupied by the exine skeleton alone and by the pollen grain was separately obtained using the RI contrast, as described in the Methods section. The results are summarized in Table 1. The volumes of the pollen grains were 86.8 ± 14.4, 91.3 ± 13.7, and 145.5 pL (mean $\pm$ standard deviation) for L. candidum, *I. domestica*, and *H. dumortieri*, respectively (Table. 1). The surface areas *S* were calculated from the isosurface of the reconstructed tomograms.

The retrieved values for the surface area were 19.9 ± 0.8, 26.3 ± 2.7, and 30.0 ($\times 10^3$ µm^2) for *L. candidum, I. domestica, and H. dumortieri*, respectively. The sphericities, calculated from the volumes and surface areas were 0.474 ± 0.034, 0.373 ± 0.030, and 0.447. The volumes of the exine structure pollen grains from different species were 31.2 ± 6.3, 28.4 ± 5.1, and 62.0 pL. The mean RI of the exine structures were 1.536, 1.536, and 1.530 for the pollen grains from *L. candidum, I. domestica, and H. dumortieri*, respectively.

Species	Exine volume (pL)	Volume (pL)	Surface area ($\times 10^3 \, \mu m^2$)	Sphericity
L. candidum	31.2 ± 6.3	86.8 ± 14.4	19.9 ± 0.8	0.474 ± 0.034
I. domestica	$28.4 \quad \pm 5.1$	91.3 ± 13.7	26.3 ± 2.7	0.373 ± 0.030
H. dumortieri	62.0	145.5	30.0	0.447

Table 1: Various physical quantities obtained from the 3D RI distribution of the pollen grains from three angiosperm species.

4. Discussion/ Conclusion

In conclusion, label-free 3D imaging and analyses of individual angiosperm pollen grains were demonstrated using ODT. The 3D RI distribution of pollen grains provided structural information including exine and pollen aperture in pollen grains from various angiosperm plants. Furthermore, through quantitative analysis of the obtained 3D RI distribution, various physical quantities including cellular volume, surface area, and exine volume were obtained.

ODT provides 3D label-free and quantitative imaging capabilities by exploiting RI distributions in the samples. Thus, we believe ODT can offer new opportunities to investigate the diverse properties of pollen grains. For instance, ODT can provide useful insights in understanding the germination procedure of pollen grains. As is well known, the plasticity of the exine wall and the aperture of a pollen grain is linked with its ability to facilitate a volume increase of a hydrated pollen grain or germination of a pollen grain [10]. Thus, quantitative information regarding the exine wall and pollen aperture may potentially be utilized to investigate the fertilization process. Furthermore, the development of a pollen tube breaking through the pollen aperture may be directly observed using ODT without labeling agents, which has been previously investigated using fluorescence microscopy [15, 18].

Even though ODT efficiently provides 3D quantitative information on a pollen grain, ODT has limited use in molecular imaging. Therefore, subcellular organelles, such as vegetative and sperm cells could not be observed directly in ODT and requires the use of fluorescence imaging techniques [58, 59]. However, the limited molecular specificity of ODT can be overcome by various modalities in ODT, including hyperspectral [60] or polarization sensitive QPI imaging [61]. Alternatively, the correlative approach combining both ODT and fluorescence imaging [62, 63] may also provide new means to study plant biology.

Funding

References

[1] M. Fenner, Seeds: the ecology of regeneration in plant communities, Cabi, 2000.
[2] R. Lewin, Fragile forests implied by Pleistocene pollen, Science, 226 (1984) 36-38.
[3] T.M. Knight, J.A. Steets, J.C. Vamosi, S.J. Mazer, M. Burd, D.R. Campbell, M.R. Dudash, M.O. Johnston, R.J. Mitchell, T.-L. Ashman, Pollen limitation of plant reproduction: pattern and process, Annu. Rev. Ecol. Evol. Syst., 36 (2005) 467-497.
[4] R.B. Knox, Pollen biotechnology for crop production and improvement, Cambridge University Press, 2005.
[5] N. Wikström, V. Savolainen, M.W. Chase, Evolution of the angiosperms: calibrating the family tree, Proceedings of the Royal Society of London B: Biological Sciences, 268 (2001) 2211-2220.
[6] G. Liu, W.K. Cornwell, X. Pan, K. Cao, X. Ye, Z. Huang, M. Dong, J.H. Cornelissen, Understanding the ecosystem implications of the angiosperm rise to dominance: leaf litter decomposability among magnoliids and other basal angiosperms, Journal of ecology, 102 (2014) 337-344.
[7] D.L. Dilcher, Early angiosperm reproduction: an introductory report, Review of Palaeobotany and Palynology, 27 (1979) 291-328.
[8] W.W. Payne, Observations of harmomegathy in pollen of Anthophyta, Grana, 12 (1972) 93-98.
[9] E. Katifori, S. Alben, E. Cerda, D.R. Nelson, J. Dumais, Foldable structures and the natural design of pollen grains, Proceedings of the National Academy of Sciences, 107 (2010) 7635-7639.
[10] A. Matamoro-Vidal, C. Raquin, F. Brisset, H. Colas, B. Izac, B. Albert, P.-H. Gouyon, Links between morphology and function of the pollen wall: an experimental approach, Botanical journal of the Linnean Society, 180 (2016) 478-490.
[11] J. Heslop-Harrison, Y. Heslop-Harrison, M. Cresti, A. Tiezzi, A. Moscatelli, Cytoskeletal elements, cell shaping and movement in the angiosperm pollen tube, Journal of Cell Science, 91 (1988) 49-60.

[12] H.-D. Behnke, Transmission electron microscopy and systematics of flowering plants, in: Flowering Plants, Springer, 1977, pp. 155-178.

[13] E. Schrank, Scanning electron and light microscopic investigations of angiosperm pollen from the Lower Cretaceous of Egypt, Pollen et Spores, (1983).

[14] S. Wang, D. Wang, Q. Wu, K. Gao, Z. Wang, Z. Wu, 3D imaging of a rice pollen grain using transmission X-ray microscopy, Journal of synchrotron radiation, 22 (2015) 1091-1095.

[15] H. Lindner, S.A. Kessler, L.M. Müller, H. Shimosato-Asano, A. Boisson-Dernier, U. Grossniklaus, TURAN and EVAN mediate pollen tube reception in Arabidopsis synergids through protein glycosylation, PLoS biology, 13 (2015) e1002139.

[16] J. Atlagić, S. Terzić, A. Marjanović-Jeromela, Staining and fluorescent microscopy methods for pollen viability determination in sunflower and other plant species, Industrial crops and products, 35 (2012) 88-91.

[17] M. Chica, Authentication of bee pollen grains in bright field microscopy by combining one class classification techniques and image processing, Microscopy research and technique, 75 (2012) 1475-1485.

[18] A.Y. Cheung, Q.-h. Duan, S.S. Costa, B.H. de Graaf, V.S. Di Stilio, J. Feijo, H.-M. Wu, The dynamic pollen tube cytoskeleton: live cell studies using actin-binding and microtubule-binding reporter proteins, Molecular plant, 1 (2008) 686-702.

[19] R. Dixit, R. Cyr, Cell damage and reactive oxygen species production induced by fluorescence microscopy: effect on mitosis and guidelines for non invasive fluorescence microscopy, The Plant Journal, 36 (2003) 280-290.

[20] L. Song, R.P.M.v. Gijlswijk, I.T. Young, H.J. Tanke, Influence of fluorochrome labeling density on the photobleaching kinetics of fluorescein in microscopy, Cytometry, 27 (1997) 213-223.

[21] K. Lee, K. Kim, J. Jung, J. Heo, S. Cho, S. Lee, G. Chang, Y. Jo, H. Park, Y. Park, Quantitative phase imaging techniques for the study of cell pathophysiology: from principles to applications, Sensors, 13 (2013) 4170-4191.

[22] Y. Park, C.A. Best, T. Kuriabova, M.L. Henle, M.S. Feld, A.J. Levine, G. Popescu, Measurement of the nonlinear elasticity of red blood cell membranes, Physical Review E, 83 (2011).

[23] D. Kim, S. Lee, M. Lee, J. Oh, S.-A. Yang, Y. Park, Refractive index as an intrinsic imaging contrast for 3-D label-free live cell imaging, bioRxiv, (2017) 106328.

[24] E. Wolf, Three-dimensional structure determination of semi-transparent objects from holographic data, Optics Communications, 1 (1969) 153-156.

[25] K. Kim, J. Yoon, S. Shin, S. Lee, S.-A. Yang, Y. Park, Optical diffraction tomography techniques for the study of cell pathophysiology, Journal of Biomedical Photonics & Engineering, 2 (2016) 020201.

[26] Y. Sung, W. Choi, C. Fang-Yen, K. Badizadegan, R.R. Dasari, M.S. Feld, Optical diffraction tomography for high resolution live cell imaging, Opt. Express, 17 (2009) 266-277.

[27] J. Yoon, S.-a. Yang, K. Kim, Y. Park, Quantification of neurotoxic effects on individual neuron cells using optical diffraction tomography (Conference Presentation), in: Quantitative Phase Imaging II, International Society for Optics and Photonics, 2016, pp. 97180L.

[28] S.A. Yang, J. Yoon, K. Kim, Y. Park, Measurements of morphological and biophysical alterations in individual neuron cells associated with early neurotoxic effects in Parkinson's disease, Cytometry part A, 91 (2017) 510-518.

[29] T. Kim, R. Zhou, M. Mir, S.D. Babacan, P.S. Carney, L.L. Goddard, G. Popescu, White-light diffraction tomography of unlabelled live cells, Nature Photonics, 8 (2014) 256-263.

[30] K. Kim, H. Yoon, M. Diez-Silva, M. Dao, R.R. Dasari, Y. Park, High-resolution three-dimensional imaging of red blood cells parasitized by Plasmodium falciparum and in situ hemozoin crystals using optical diffraction tomography, in, SPIE, 2013, pp. 12.

[31] Y. Kim, H. Shim, K. Kim, H. Park, S. Jang, Y. Park, Profiling individual human red blood cells using common-path diffraction optical tomography, Scientific reports, 4 (2014) 6659.

[32] K. Kim, K.S. Kim, H. Park, J.C. Ye, Y. Park, Real-time visualization of 3-D dynamic microscopic objects using optical diffraction tomography, Opt. Express, 21 (2013) 32269-32278.

[33] G. Kim, M. Lee, S. Youn, E. Lee, D. Kwon, J. Shin, S. Lee, Y.S. Lee, Y. Park, Measurements of three-dimensional refractive index tomography and membrane deformability of live erythrocytes from Pelophylax nigromaculatus, Scientific Reports, 8 (2018) 9192.

[34] A. Liutkus, D. Martina, S. Popoff, G. Chardon, O. Katz, G. Lerosey, S. Gigan, L. Daudet, I. Carron, Imaging with nature: Compressive imaging using a multiply scattering medium, Scientific reports, 4 (2014) 5552.

[35] S. Shin, K. Kim, T. Kim, J. Yoon, K. Hong, J. Park, Y. Park, Optical diffraction tomography using a digital micromirror device for stable measurements of 4D refractive index tomography of cells, in: Quantitative Phase Imaging II, International Society for Optics and Photonics, 2016, pp. 971814.

[36] Y. Kim, H. Shim, K. Kim, H. Park, J.H. Heo, J. Yoon, C. Choi, S. Jang, Y. Park, Common-path diffraction optical tomography for investigation of three-dimensional structures and dynamics of biological cells, Opt. Express, 22 (2014) 10398-10407.

[37] K. Kim, J. Yoon, Y. Park, Simultaneous 3D visualization and position tracking of optically trapped particles using optical diffraction tomography, Optica, 2 (2015) 343-346.

[38] Y. Cotte, F. Toy, P. Jourdain, N. Pavillon, D. Boss, P. Magistretti, P. Marquet, C. Depeursinge, Marker-free phase nanoscopy, Nature Photonics, 7 (2013) 113.

[39] T.I. Kim, B. Kwon, J. Yoon, I.-J. Park, G.S. Bang, Y. Park, Y.-S. Seo, S.-Y. Choi, Antibacterial Activities of Graphene Oxide–Molybdenum Disulfide Nanocomposite Films, ACS Applied Materials & Interfaces, 9 (2017) 7908-7917.

[40] M. Bennet, D. Gur, J. Yoon, Y. Park, D. Faivre, A Bacteria Based Remotely Tunable Photonic Device, Advanced Optical Materials, 5 (2017).

[41] M. Habaza, B. Gilboa, Y. Roichman, N.T. Shaked, Tomographic phase microscopy with 180 rotation of live cells in suspension by holographic optical tweezers, Optics letters, 40 (2015) 1881-1884.

[42] J. Jung, S.-J. Hong, H.-B. Kim, G. Kim, M. Lee, S. Shin, S. Lee, D.-J. Kim, C.-G. Lee, Y. Park, Label-free non-invasive quantitative measurement of lipid contents in individual microalgal cells using refractive index tomography, bioRxiv, (2017).

[43] G. Kim, S. Lee, S. Shin, Y. Park, Three-dimensional label-free imaging and analysis of Pinus pollen grains using optical diffraction tomography, Scientific Reports, 8 (2018) 1782.

[44] K. Lee, K. Kim, G. Kim, S. Shin, Y. Park, Time-multiplexed structured illumination using a DMD for optical diffraction tomography, Optics letters, 42 (2017) 999-1002.

[45] M. Takeda, H. Ina, S. Kobayashi, Fourier-transform method of fringe-pattern analysis for computer-based topography and interferometry, JosA, 72 (1982) 156-160.

[46] V. Lauer, New approach to optical diffraction tomography yielding a vector equation of diffraction tomography and a novel tomographic microscope, Journal of Microscopy, 205 (2002) 165-176.

[47] C. Park, S. Shin, Y. Park, Generalized quantification of three-dimensional resolution in optical diffraction tomography using the projection of maximal spatial bandwidths, arXiv preprint arXiv:1806.01067, (2018).

[48] J. Lim, K. Lee, K.H. Jin, S. Shin, S. Lee, Y. Park, J.C. Ye, Comparative study of iterative reconstruction algorithms for missing cone problems in optical diffraction tomography, Opt. Express, 23 (2015) 16933-16948.

[49] K. Kim, H. Yoon, M. Diez-Silva, M. Dao, R.R. Dasari, Y. Park, High-resolution three-dimensional imaging of red blood cells parasitized by Plasmodium falciparum and in situ hemozoin crystals using optical diffraction tomography, J Biomed Opt, 19 (2014).

[50] W.M. bin Mat Yunus, A. bin Abdul Rahman, Refractive index of solutions at high concentrations, Applied optics, 27 (1988) 3341-3343.

[51] M. Borg, D. Twell, Pollen: structure and development, eLS, (2011).

[52] S. BLACKMORE, S.H. BARNES, Harmomegathic mechanisms in pollen grains, in: Linnean Society symposium series, Academic Press, 1986, pp. 137-149.

[53] R.P. Wodehouse, Pollen grains: Their structure, identification and significance in science and medicine, The Journal of Nervous and Mental Disease, 86 (1937) 104.

[54] J. Brooks, G. Shaw, Sporopollenin: a review of its chemistry, palaeochemistry and geochemistry, Grana, 17 (1978) 91-97.

[55] J.J. Skvarla, J.W. Nowicke, Ultrastructure of pollen exine in centrospermous families, Plant Systematics and Evolution, 126 (1976) 55-78.

[56] C.A. Furness, P.J. Rudall, Pollen aperture evolution–a crucial factor for eudicot success?, Trends in plant science, 9 (2004) 154-158.

[57] J.W. Walker, Evolution of exine structure in the pollen of primitive angiosperms, American Journal of Botany, 61 (1974) 891-902.

[58] K. von Besser, A.C. Frank, M.A. Johnson, D. Preuss, Arabidopsis HAP2 (GCS1) is a sperm-specific gene required for pollen tube guidance and fertilization, Development, 133 (2006) 4761-4769.

[59] S. Miyamura, T. Kuroiwa, T. Nagata, Disappearance of plastid and mitochondrial nucleoids during the formation of generative cells of higher plants revealed by fluorescence microscopy, Protoplasma, 141 (1987) 149-159.

[60] J. Jung, K. Kim, J. Yoon, Y. Park, Hyperspectral optical diffraction tomography, Opt. Express, 24 (2016) 2006-2012.

[61] Z. Wang, L.J. Millet, M.U. Gillette, G. Popescu, Jones phase microscopy of transparent and anisotropic samples, Optics letters, 33 (2008) 1270-1272.

[62] S. Shin, D. Kim, K. Kim, Y. Park, Super-resolution three-dimensional fluorescence and optical diffraction tomography of live cells using structured illumination generated by a digital micromirror device, Scientific Reports, 8 (2018) 9138.

[63] K. Kim, W.S. Park, S. Na, S. Kim, T. Kim, W. Do Heo, Y. Park, Correlative three-dimensional fluorescence and refractive index tomography: bridging the gap between molecular specificity and quantitative bioimaging, Biomedical optics express, 8 (2017) 5688-5697.